Electronic Supplementary Material

A pseudocapacitive molecule-induced strategy to construct flexible high-performance asymmetric supercapacitors

Yingqi Heng[1], Xiang Qin[1], Heng Fang[1], Genhui Teng[1], Dawei Zhao[2], Dongying Hu (✉)[1, 3]

1 School of Resources, Environment and Materials, Guangxi University, Nanning, 530004, China

2 Key Laboratory on Resources Chemicals and Materials of Ministry of Education, Shenyang University of Chemical Technology, Shenyang 110142, China

3 State Key Laboratory of Featured Metal Materials and Life-cycle Safety for Composite Structures, Guangxi University, Nanning 530004, China

E-mails: hdy@gxu.edu.cn; hdygxu@163.com

The CV curves of different samples at 5 mV s^{-1} in Figure S1a show that GO-150 exhibits a typical bilayer rectangle, while LG-150 exhibits a very obvious redox peak, which greatly increases the integral area of the CV curve, which proves that SL contributes pseudocapacitance to the LG-150 electrode. The calculated Cg of the GO-150, LG-150 and LGP-150 electrodes are 89, 137, and 264 F g^{-1} at 5 mV s^{-1}, respectively, which also demonstrates that the introduction of SL greatly enhances the specific capacitance values through rapid and reversible redox reactions. When PANI is added, the CV area is further increased, so the LGP-150 electrode has better electrochemical performance. This result is due to the in situ polymerization of PANI in an acidic environment, which greatly increases the reaction sites and forms shorter conductive pathways, thereby enhancing the electrochemical performance. Figure S1b

shows the GCD curves of GO-150, LG-150 and LGP-150 electrodes at 1 A g^{-1}. It can be seen that the GO-150 electrode exhibits a linear isosceles triangular curve, indicating a stable double-layer energy storage behavior, while the LG-150 and LGP-150 electrodes exhibit a nonlinear isosceles triangular-like shape with slow charging and discharging plateaus indicating the presence of pseudocapacitive energy storage behavior, which is consistent with the CV curves. The above results are further demonstrated in the EIS curves of Figure S1c, where the LGP-150 electrode has smaller Rs and Rct compared with GO-150 and LG-150, proving that it has the best charge transfer capability and the smallest resistance performance among the three of them. Figure S1d shows the specific capacitance curves of GO-150, LG-150 and LGP-150 composite electrodes in the range of 0.5 to 5 A g^{-1}. The specific capacitances at 0.5 A g^{-1} are 106, 201 and 521 F g^{-1}, and at 5 A g^{-1} are 68, 146 and 390 F g^{-1}, respectively, and the capacitance retention rates are 64.2 %, 72.6 % and 74.9 %, respectively. The results indicate that the LGP-150 electrode has the largest specific capacitance and the highest capacitance retention, which is consistent with the results of CV and GCD curves, proving that the addition of SL and PANI provides the pseudocapacitance, respectively, making the LG-150 and LGP-150 electrodes display a specific capacitance far exceeding that of the GO-150 electrode.

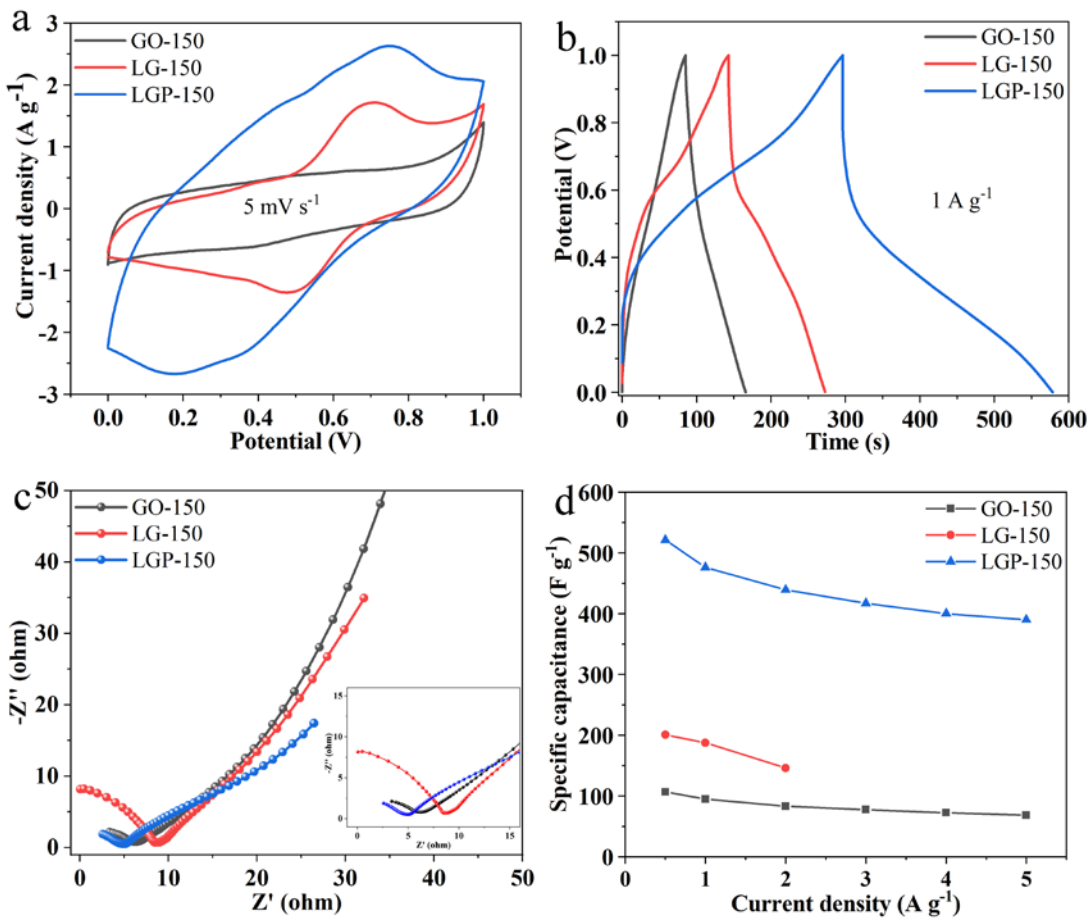

Figure S1. The electrochemical performance of the GO-150, LG-150, and LGP-150 electrodes: (a) CV curves at 5 mV s^{-1}, (b) GCD curves at 1 A g^{-1}, (c) Nyquist plots (the inset shows a magnified view of the high-frequency region), and (d) specific capacitance curves in the range of 0.5 to 5 A g^{-1}

Temperature favors the acceleration of molecular motions, which affects the strength of the cross-linking reaction. To investigate the effect of hydrothermal temperature on the electrochemical properties, the electrochemical properties of the composites prepared at five different hydrothermal temperatures including 80 °C, 100 °C, 120 °C, 150 °C and 180 °C is investigated. The electrochemical properties are shown in Figure S2. The specific capacitances at 0.5 A g^{-1} of the five electrode

materials, LGP-80, LGP-100, LGP-120, LGP-150 and LGP-180, are 425, 412, 514, 521 and 184 F g^{-1}, and at 5 A g^{-1} are 303, 252, 120, 390 and 113 F g^{-1}, respectively. The capacitance retention rates are 71.3 %, 61.2 %, 23.3 %, 74.9 % and 61.4 %, respectively, indicating that the LGP-150 electrode has the largest specific capacitance and the highest capacitance retention rate. With the increase of temperature, the adhesion between PANI and LG film may become closer, and the best adhesion effect is achieved at 150 ℃, suggesting the most robust conductive structure. When the temperature is increased to 180 ℃, the binding effect between PANI and LG may become worse, and the electrochemical performance is greatly reduced. This indicates that 150 °C is the optimum water heating temperature.

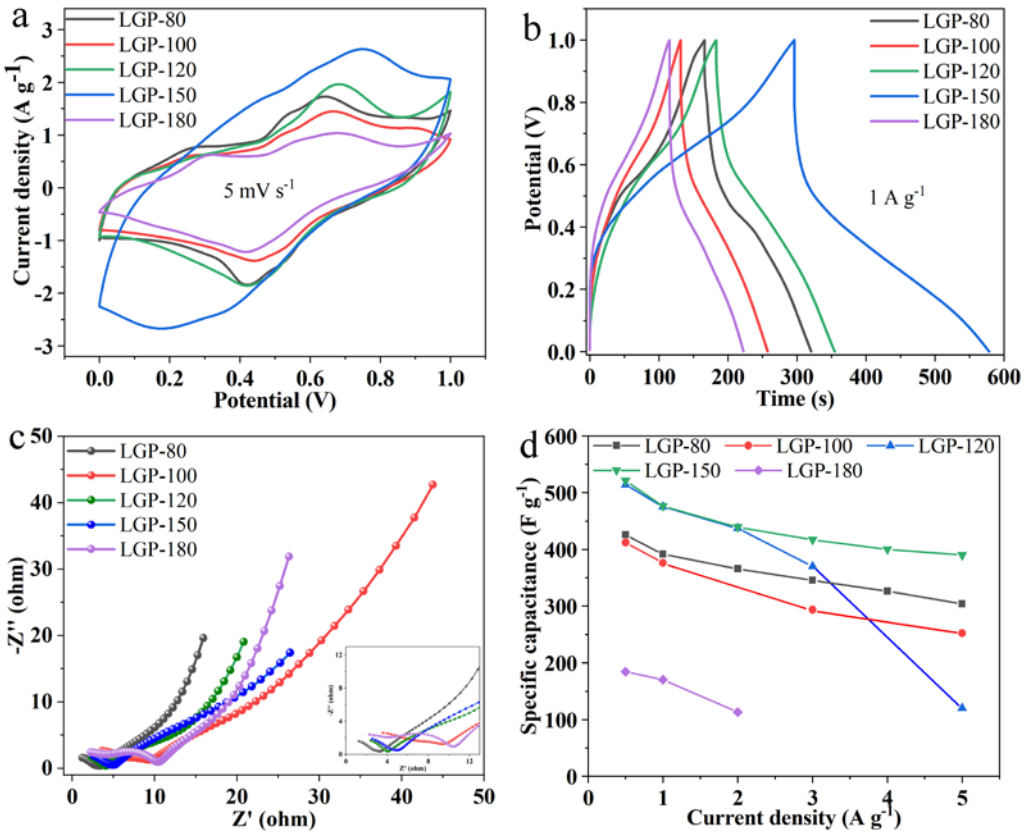

Figure S2. The electrochemical performance of LGP-80, LGP-100, LGP-120, LGP-150, and LGP-180 electrodes: (a) CV curves at 5 mV s^{-1}, (b) GCD curves at 1 A

g^{-1}, (c) Nyquist plots (the inset shows a magnified view of the high-frequency region), and (d) specific capacitance curves in the range of 0.5 to 5 A g^{-1}

In order to clarify the effect of PANI polymerization time, five electrodes were obtained by controlling the PANI polymerization time of 3 h, 6 h, 9 h, 12 h and 15 h to further discuss the electrochemical properties. Figure S3a shows the CV curves of the LGP-150 electrode at 5 mV s^{-1}. Comparing the closed areas of the curves, the CV curves with the polymerization time of 12 h have the largest closed areas, and the specific capacitances are calculated to be 159, 156, 243, 264, and 231 F g^{-1}, indicating that 12 h is the optimal polymerization time. The CV curves have a pair of distinct redox peaks, which can be attributed to the pseudocapacitance provided by the phenoquinone group in SL and the biphenyl and benzoquinone units in PANI. Figure S5b shows the GCD curves of the samples prepared at different polymerization times at 1 A g^{-1}. It can be seen that all curves exhibit an obvious slow discharge plateau, which proves the pseudocapacitance storage mechanism, and the pattern of 12h > 9h > 15h > 6h > 3h can be obtained by the discharge duration, which is basically consistent with the CV curve results. Figure S3c shows the EIS of all electrode materials, and it can be seen that the EIS plots with polymerization time of 9 h, 12 h and 15 h all show very small Rs and Rct in the high frequency region, while the electrode at 12 h polymerization time has the maximum slope in the low frequency region, which indicates its best ion diffusion ability. Figure S3d shows the specific capacitance curves of the five composite electrodes in the range of 0.5 to 5 A g^{-1}. The

specific capacitances are 288, 391, 400, 521 and 401 F g^{-1} at 0.5 A g^{-1}, and 157, 204, 250, 390 and 273 F g^{-1} at 5 A g^{-1}, respectively. Their capacitance retention rates are 54.5 %, 52.3 %, 62.5 %, 74.9 %, and 68.1 %. The results show that the electrodes obtained by 12 h polymerization had the highest specific capacitance and the highest capacitance retention, which are consistent with the CV and GCD curves, proving that 12 h was the optimum polymerization time.

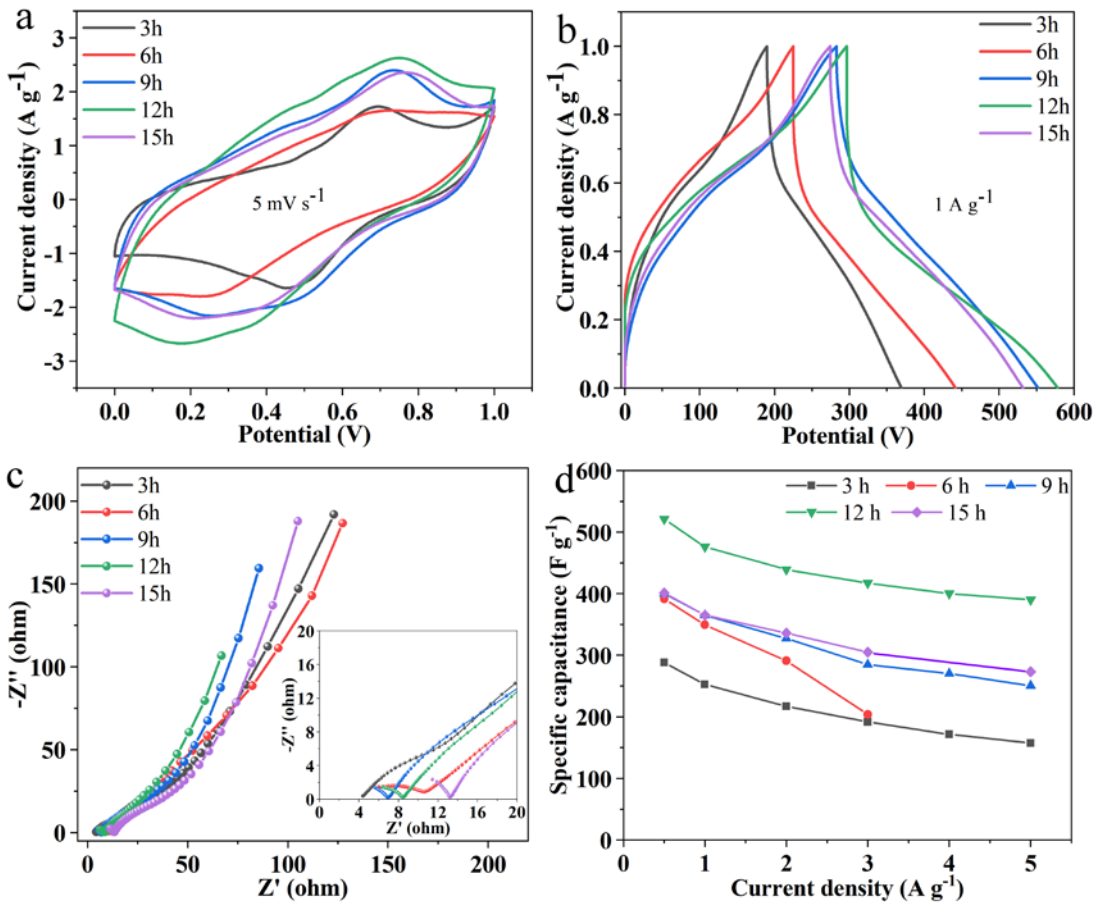

Figure S3. The electrochemical performance of the GO-150, LG-150, and LGP-150 electrodes: (a) CV curves at 5 mV s^{-1}, (b) GCD curves at 1 A g^{-1}, (c) Nyquist plots (the inset shows a magnified view of the high-frequency region), and (d) specific capacitance curves in the range of 0.5 to 5 A g^{-1}

Table S1. Comparison of specific capacitances in three-electrode systems.

Work Electrode	Reference electrodes	Cg ($F\ g^{-1}$)	Electrolyte	ΔV	Ref
Ti_3C_2/rGO	Ag/AgCl	254 (2 mV s^{-1})	1 M H_2SO_4	-0.3~0.4 V	[S1]
Ti_3C_2Tx/HCNF@Lig(3@1)$_{97/3}$	Ag/AgCl	272 (0.5 A g^{-1})	1 M H_2SO_4	-0.35~0.4 V	[S2]
Grafted PANI/GO	$Hg/HgCl_2$	442 (1 A g^{-1})	1 M H_2SO_4	0~0.8 V	[S3]
GPH7	Ag/AgCl	375 (1 A g^{-1})	2 M H_2SO_4	-0.2~0.6 V	[S4]
rGO/PANI film	Ag/AgCl	385 (0.5 A g^{-1})	1 M H_2SO_4	0~1 V	[S5]
PANI/graphene Hydrogel	Ag/AgCl	224 (0.4 A g^{-1})	H_2SO_4/HQ	0~0.8 V	[S6]
rGO/CNT/PANI paper	$Hg/HgCl_2$	257 (0.2 A g^{-1})	1 M H_2SO_4	-0.65~0.35 V	[S7]
Lig/SWCNT$_{HNO3}$	$Hg/HgCl_2$	372 (1 A g^{-1})	1 M Li_2SO_4	-0.3~0.7 V	[S8]
Lignin/Ti_3C_2/i-PANI/Ti_3C_2	Ag/AgCl	240 (1 A g^{-1})	1 M H_2SO_4	-0.35~0.2V	[S9]
LG-150	Ag/AgCl	201 (0.5 A g^{-1})	1 M H_2SO_4	0~1 V	This work

LGP-150	Ag/AgCl	521 (0.5 A g^{-1})	1 M H_2SO_4	0~1 V	This work

Table S2. A performance comparison of this work with that of symmetric ASSSCs reported.

Electrode	**C'g (F g^{-1})**	**Cycle ability**	**E (Wh kg^{-1})**	**P (kW kg^{-1})**	**Ref**
Modified PANI@OGH film	530 (0.5 A g^{-1})	80% (3k)	8.12	19.71	[S10]
RL-60	203 (1 A g^{-1})	96.1% (3k)	10	40	[S11]
Lig/SWCNT-HNO_3 hydrogels	292 (0.5 A g^{-1})	78.3% (3k)	17.1	0.324	[S8]
PANI/CNT	322 (1 A g^{-1})	91.9% (1k)	7.1	2.2	[S12]
FrGO/PANI	324.4 (1 A g^{-1})	83.3% (1k)	16.3	0.3	[S13]
rGO@MnO_2/PANI	125 (1 A g^{-1})	83.9% (5k)	18.3	0.4	[S14]
LS-GHS	408 (1 A g^{-1})	84% (10k)	13.8	0.5	[S15]

Hydrothermal rGO	186 ($1\ A\ g^{-1}$)	92% (2k)	6.1	0.67	[S16]
Hydrazine rGO	220 ($1\ A\ g^{-1}$)	91.6% (10k)	7.2	0.5	[S17]
Graphene paper	80 ($1\ A\ g^{-1}$)	100% (10k)	8.8	0.18	[S18]
Nanocellulose/PANI/ rGO	79.7 ($0.1\ A\ g^{-1}$)	—	5.09	0.15	[S19]
PANI-LS	227 ($1\ A\ g^{-1}$)	87% (15k)	14.5	26	[S20]
Lignin/PAN nanofiber	129.2 ($0.5\ A\ g^{-1}$)	95% (10k)	4.49	2.63	[S21]
PErGO-based	81 ($0.5\ A\ g^{-1}$)	94.5% (5k)	11.25	5	[S22]
rGO@Fe_3O_4@PANI	283.4 ($1\ A\ g^{-1}$)	78% (5k)	47.7	0.5	[S23]
LECP/PANI gel	184 ($0.5\ A\ g^{-1}$)	74% (1k)	3	0.0416	[S24]
LG-150	123.6 ($1\ A\ g^{-1}$)	100% (10k)	40.92	3	This work
LGP-150	185 ($1\ A\ g^{-1}$)	81.4% (10k)	54.58	3	This work

Table S3. A performance comparison of this work with that of asymmetric ASSSCs reported.

Electrode		C'g (F g^{-1})	Cycle ability	E (Wh kg^{-1})	P (kW kg^{-1})	Ref
Positive	Negative					
GO@Zn-Co-Ni	AC	837 (1 A g^{-1})	97.1% (5k)	64.91	0.8	[S25]
AC/lig-MnO_2	AC	12 (6 mA g^{-1})	97.5% (2k)	14.11	1	[S26]
e-CMG	MnO_2/e-CMG	—	95% (1k)	44	11.2	[S27]
rGO@Mn_3O_4	rGO@VO_2	98 (0.4 A g^{-1})	82% (10k)	42.7	0.3	[S28]
PANI@Mn_3O_4	AC	100.2 (0.36 A g^{-1})	-	40.2	0.34	[S29]
$Ni(OH)_2$/UGF	a-MEGO	119 (1 A g^{-1})	63.2% (10k)	13.4	85	[S30]
10-graphene-WO_3	AC	171 (1 A g^{-1})	93.6% (4k)	26.7	6	[S31]
aGNS/cMWCNT/PANI	aGNS	107 (1 A g^{-1})	91.4% (5k)	41.5	0.17	[S32]
Fe_3O_4/graphene	$CoFe_2O_4$/graphene	114 (1 A g^{-1})	91% (5k)	45.5	0.84	[S33]

LGP-150	LG-150	209 ($1\ A\ g^{-1}$)	101% (5k)	83.87	3.4	This work

REFERENCES

[S1] Navarro-Suárez AM, Maleski K, Makaryan T, Yan J, Anasori B, Gogotsi Y. 2D titanium carbide/reduced graphene oxide heterostructures for supercapacitor applications. Batteries & Supercaps, 2018, 1 (1): 33-38

[S2] Chang L, Peng Z, Zhang T, Yu C, Zhong W. Nacre-inspired composite films with high mechanical strength constructed from MXenes and wood-inspired hydrothermal cellulose-based nanofibers for high performance flexible supercapacitors. Nanoscale, 2021, 13 (5): 3079-3091

[S3] Wu D, Zhong W. A new strategy for anchoring a functionalized graphene hydrogel in a carbon cloth network to support a lignosulfonate/polyaniline hydrogel as an integrated electrode for flexible high areal-capacitance supercapacitors. Journal of Materials Chemistry A, 2019: 7 (10): 5819-5830

[S4] Li Z-F, Zhang H, Liu Q, Liu Y, Stanciu L, Xie J. Covalently-grafted polyaniline on graphene oxide sheets for high performance electrochemical supercapacitors. Carbon, 2014, 71: 257-267

[S5] Meng Y, Wang K, Zhang Y, Wei Z. Hierarchical porous graphene/polyaniline composite film with superior rate performance for flexible supercapacitors, Advanced Materials, 2013, 25 (48): 6985-6990

[S6] Moussa M, Zhao Z, El-Kady MF, Liu H, Michelmore A, Kawashima N, et al. Free-standing composite hydrogel films for superior volumetric capacitance. Journal

of Materials Chemistry A, 2015, 3 (30): 15668-15674

[S7] Huang ZD, Liang R, Zhang B, He Y-B, Kim J-K. Evolution of flexible 3D graphene oxide/carbon nanotube/polyaniline composite papers and their supercapacitive performance. Composites Science and Technology, 2013, 88: 126-133

[S8] Peng Z, Zou Y, Xu S, Zhong W, Yang W. High-performance biomass-based flexible solid-state supercapacitor constructed of pressure-sensitive lignin-based and cellulose hydrogels. ACS Applied Materials & Interfaces, 2018, 10 (26): 22190-22200

[S9] Zhou Y, Zou Y, Peng Z, Yu C, Zhong W. Arbitrary deformable and high-strength electroactive polymer/MXene anti-exfoliative composite films assembled into high performance, flexible all-solid-state supercapacitors. Nanoscale, 2020, 12: 20797-20810

[S10] Du P, Liu HC, Yi C, Wang K, Gong X. Polyaniline-modified oriented graphene hydrogel film as the free-standing electrode for flexible solid-state supercapacitors. ACS Applied Materials & Interfaces, 2015, 7 (43): 23932-23940

[S11] Kim S-K, Kim YK, Lee H, Lee SB, Park HS. Back cover: superior pseudocapacitive behavior of confined lignin nanocrystals for renewable energy-storage materials. ChemSusChem, 2014, 7 (4): 1196-1196

[S12] Dai L, Ma M, Xu J, Si C,Wang X, Liu Z, et al. All-lignin-based hydrogel with fast pH-stimuli responsiveness for mechanical switching and actuation. Chemistry of Materials, 2020, 32 (10): 4324-4330

[S13] Jin K, Zhang W, Wang Y, Guo X, Chen Z, Li L, et al. In–situ hybridization of polyaniline nanofibers on functionalized reduced graphene oxide films for high-performance supercapacitor. Electrochimica Acta, 2018, 285: 221-229

[S14] Ghosh K, Yue CY. Development of 3D MoO_3/graphene aerogel and sandwich-type polyaniline decorated porous MnO_2−graphene hybrid film based high performance all-solid-state asymmetric supercapacitors. Electrochimica Acta, 2018, 276: 47-63

[S15] Li F, Xiluan W, Sun R-C. A metal-free and flexible supercapacitor based on redox-active lignosulfonate functionalized graphene hydrogels. Journal of Materials Chemistry A, 2017, 5: 20643-20650

[S16] Xu Y, Lin Z, Huang X, Liu Y, Huang Y, Duan X. Flexible solid-state supercapacitors based on three-dimensional graphene hydrogel films. ACS Nano, 2013, 7 (5): 4042-4049

[S17] Zhang L, Shi G. Preparation of highly conductive graphene hydrogels for fabricating supercapacitors with high-rate capability. Journal of Physical Chemistry C, 2011, 115: 17206-17212

[S18] Ramadoss A, Yoon K-Y, Kwak M-J, Kim S-I, Ryu S-T, Jang J.-H. Fully flexible, lightweight, high performance all-solid-state supercapacitor based on 3-Dimensional-graphene/graphite-paper. Journal of Power Source, 2017, 337: 159-165

[S19] Hsu HH, Khosrozadeh A, Li B, Luo G, Xing M, Zhong W. An eco-friendly, nanocellulose/RGO/in situ formed polyaniline for flexible and free-standing

supercapacitors, ACS Sustainable Chemistry & Engineering, 2019, 7 (5): 4766-4776

[S20] Dianat N, Rahmanifar MS, Noori A, El-Kady MF, Chang X, Kaner RB, et al. Polyaniline-lignin interpenetrating network for supercapacitive energy storage. Nano Letters, 2021, 21: 9485-9493

[S21] Park JH, Rana HH, Lee JY, Park HS. Renewable flexible supercapacitors based on all-lignin-based hydrogel electrolytes and nanofiber electrodes, Journal of Materials Chemistry A, 2019, 7 (28): 16962-16968

[S22] Purkait T, Singh G, Singh M, Kumar D, Dey RS. Large area few-layer graphene with scalable preparation from waste biomass for high-performance supercapacitor. Scientific Reports, 2017, 7: 15239

[S23] Mondal S, Rana U, Malik S. Reduced graphene oxide/Fe_3O_4/polyaniline nanostructures as electrode materials for an all-solid-state hybrid supercapacitor. Journal of Physical Chemistry C, 2017, 121: 7573-7583

[S24] Zhao H-B, Yuan L, Fu Z-B, Wang C-Y, Yang X, Zhu J-Y, et al. Biomass-based mechanically strong and electrically conductive polymer aerogels and their application for supercapacitors. ACS Applied Materials & Interfaces, 2016, 8 (15): 9917-9924

[S25] Zhu L, Chen H, Wang X, Guo Y. Fluffy cotton-like GO/Zn-Co-Ni layered double hydroxides form from a sacrificed template GO/ZIF-8 for high performance asymmetric supercapacitors. ACS Sustainable Chemistry & Engineering, 2020, 8: 11618-11629

[S26] Jha S, Mehta S, Chen Y, Ma L, Renner P, Parkinson DY, et al. Correction to

"design and synthesis of lignin-based flexible supercapacitors". ACS Sustainable Chemistry & Engineering, 2020, 8 (25): 9597-9598

[S27] Choi BG, Yang M, Hong WH, Choi JW, Huh YS. 3D macroporous graphene frameworks for supercapacitors with high energy and power densities. ACS Nano, 2012, 6 (5): 4020-4028

[S28] Sahoo R, Pham DT, Lee TH, Luu THT, Seok J, Lee YH. Redox-driven route for widening voltage window in asymmetric supercapacitor. ACS Nano, 2018, 12 (8): 8494-8505

[S29] Liu N, Su Y, Wang Z, Wang Z, Xia J, Chen Y, et al. Electrostatic-interaction-assisted construction of 3D networks of manganese dioxide nanosheets for flexible high-performance solid-state asymmetric supercapacitors. ACS Nano, 2017, 11 (8): 7879-7888

[S30] Ji J, Zhang LL, Ji H, Li Y, Zhao X, Bai X, et al. Nanoporous $Ni(OH)_2$ thin film on 3D ultrathin-graphite foam for asymmetric supercapacitor. ACS Nano, 2013, 7 (7): 6237-6243

[S31] Nayak AK, Das AK, Pradhan D. High performance solid-state asymmetric supercapacitor using green synthesized graphene–WO_3 nanowires nanocomposite. ACS Sustainable Chemistry & Engineering, 2017, 5: 10128-10138

[S32] Shen J, Yang C, Li X, Wang G. High-performance asymmetric supercapacitor based on nanoarchitectured polyaniline/graphene/carbon nanotube and activated graphene electrodes. ACS Applied Materials & Interfaces, 2013, 5: 8467-8476

[S33] Wang H, Song Y, Ye X, Wang H, Liu W, Yan L. Asymmetric supercapacitors

assembled by dual spinel ferrites@graphene nanocomposites as electrodes, ACS Applied Energy Materials, 2018, 1 (7): 206-3215